Scale-Dependent Fracture-Matrix Interactions And Their Impact on Radionuclide Transport

Final Report

DE-FG02-08ER64695

September 15, 2008 - March 31, 2014

Russell L. Detwiler
Departement of Civil and Environmental Engineering
University of California, Irvine
844C Engineering Tower
Irvine, CA 92697-2175

June 30, 2014

Executive Summary

Matrix diffusion and adsorption within a rock matrix are widely regarded as important mechanisms for retarding the transport of radionuclides and other solutes in fractured rock (e.g., Neretnieks, 1980; Tang et al., 1981; Maloszewski and Zuber, 1985; Novakowski and Lapcevic, 1994; Jardine et al., 1999; Zhou and Xie, 2003; Reimus et al., 2003a,b). When remediation options are being evaluated for old sources of contamination, where a large fraction of contaminants reside within the rock matrix, slow diffusion out of the matrix greatly increases the difficulty and timeframe of remediation. Estimating the rates of solute exchange between fractures and the adjacent rock matrix is a critical factor in quantifying immobilization and/or remobilization of DOE-relevant contaminants within the subsurface. In principle, the most rigorous approach to modeling solute transport with fracture-matrix interaction would be based on local-scale coupled advection-diffusion/dispersion equations for the rock matrix and in discrete fractures that comprise the fracture network (Discrete Fracture Network and Matrix approach, hereinafter referred to as DFNM approach), fully resolving aperture variability in fractures and matrix property heterogeneity. However, such approaches are computationally demanding, and thus, many predictive models rely upon simplified models. These models typically idealize fracture rock masses as a single fracture or system of parallel fractures interacting with slabs of porous matrix or as a mobile-immobile or multi-rate mass transfer system. These idealizations provide tractable approaches for interpreting tracer tests and predicting contaminant mobility, but rely upon a fitted effective matrix diffusivity or mass-transfer coefficients. However, because these fitted parameters are based upon simplified conceptual models, their effectiveness at predicting long-term transport processes remains uncertain. Evidence of scale dependence of effective matrix diffusion coefficients obtained from tracer tests highlights this point and suggests that the underlying mechanisms and relationship between rock and fracture properties are not fully understood in large complex fracture networks. In this project, we developed a high-resolution DFN model of solute transport in fracture networks to explore and quantify the mechanisms that control transport in complex fracture networks and how these may give rise to observed scale-dependent matrix diffusion coefficients. Results demonstrate that small scale heterogeneity in the flow field caused by local aperture variability within individual fractures can lead to long-tailed breakthrough curves indicative of matrix diffusion, even in the absence of interactions with the fracture matrix. Furthermore, the temporal and spatial scale dependence of these processes highlights the inability of short-term tracer tests to estimate transport parameters that will control long-term fate and transport of contaminants in fractured aquifers.

1 Introduction

Quantifying the long-term fate of contaminants in fractured rock is a challenging problem with implications for nuclear waste storage (Reimus et al., 2003b; Hodgkinson et al., 2009) and contaminant remediation in fractured aquifers (Dearden et al., 2013). Breakthrough curves from field-scale tracer tests often exhibit early initial arrival times, multiple peaks, and long power-law tails (Hoehn et al., 1998; Becker and Shapiro, 2000; Kurtzman et al., 2007). Such breakthrough curves defy description using the classical advection-dispersion equation. Early initial arrival of solute and multiple peaks can be explained by the presence of a small number of preferential flow paths. Such flow paths occur within individual fractures due to aperture variability and at the network scale due to interconnected, high-transmissivity fractures. For conservative (non-sorbing) solutes, long-tailed, non-Fickian breakthrough curves are often attributed to the influence of diffusion into the porous rock matrix adjacent to fractures (Maloszewski et al., 2003; Reimus et al., 2003a).

In fractured rocks, matrix permeability is often negligible compared to fracture permeability (e.g., smaller by several orders of magnitude). This results in a 'dual porosity' system in which the fractures serve as transport pathways and the matrix is an immobile zone that solutes enter and exit by diffusion. Analytical solutions for dual-porosity single fractures that include advection and longitudinal dispersion within the fracture and molecular diffusion in the matrix provide a means of predicting breakthrough curves (e.g., Tang et al., 1981; Rasmuson and Neretnieks, 1981; Grisak and Pickens, 1981). Fitting these analytical models to breakthrough curves measured during laboratory studies in single fractures results in estimates of matrix diffusion coefficients (e.g. Callahan et al., 2000; Maloszewski and Zuber, 1990; Dai et al., 2012). A characteristic of these breakthrough curves is a power-law tail with a slope of $-3/2$.

Success with interpreting laboratory experiments using simple analytical models motivated the use of these models for interpreting field-scale tracer tests (Zhou et al., 2007; Reimus et al., 2011). These models also suggest that, in fractured systems where matrix diffusion is prevalent, breakthrough curves for solutes with different diffusion coefficients should exhibit distinct separation of the tails. Tracer tests using tracers with distinctly different molecular diffusion coefficients in fractured saprolite (Jardine et al., 1999) and fractured granite (Reimus et al., 2003a) both exhibited clear evidence of matrix diffusion. A tracer test in a different fractured granite (Becker and Shapiro, 2000) exhibited a long-tailed breakthrough curve that could be fit well by a single fracture matrix diffusion model, but results showed no significant separation of breakthrough curves for different solutes suggesting negligible influence of diffusive processes on the large-scale transport behavior.

Zhou et al. (2007) presented calculations of matrix diffusion coefficients for field-scale tracer tests carried out at scales ranging from 10 to 10^4 meters. Their results show that the effective matrix diffusion coefficients required to explain the observations is scale dependent and often many orders of magnitude larger than the molecular diffusion coefficient. These results further support the idea that the non-Fickian behavior observed in tracer tests in fractured systems cannot be completely attributed to matrix diffusion, and that advective

processes cannot be ignored.

Park et al. (2003) demonstrated that pressure gradients along the intersections of parallel-plate fractures can lead to 'flow cells' or advective loops within fractures in which there is no net pressure gradient across the fracture. These advective loops result in increased residence time of a fraction of solute as it travels through the system by advection alone. These results suggest a potential mechanism for advection-induced non-Fickian transport in fracture networks.

Recent efforts to incorporate both advective and diffusive processes into transport models use different approaches for representing multiple interacting continua within the fractured system (Wang et al., 2013). These models represent active fractures, inactive fractures (e.g., fractures that are connected to the network but with no net advection), and the porous matrix as distinct continua, each with transport properties that are representative of the respective continuum. However, the models of transport within each continuum require parameters to quantify the rates of transport and the rates of exchange between interacting continua. Thus, though such models are capable of fitting observed data, they do not provide a mechanistic prediction of transport through a complex system consisting of multiple interacting continua.

A mechanistic approach, which directly represents advective and diffusive processes over a broad hierarchy of length scales provides the ability to explicitly represent the transport processes within the fracture network and quantify the relative influence of geometric characteristics of a fracture network advective-diffusive transport processes. We use a large-scale three-dimensional discrete fracture network to simulate transport through fracture networks consisting of thousands of variable-aperture fractures. Because this model explicitly represents transport mechanisms over the full range of length scales, it requires no fitted mass transfer parameters and provides a means for directly relating the behavior of measured breakthrough curves to the details of the fracture network.

2 Computational model development

To explore the influence of local transport processes on network-scale observations of solute transport, we developed a high-resolution model of solute transport in discrete fracture networks. The model explicitly represents the small-scale features (i.e., aperture variability) and the physics that control fluid and solute transport within individual fractures within networks consisting of tens of thousands of fractures and thus we call the model Variable Aperture Solute Transport - Discrete Fracture Network (VAST-DFN) model. This section describes the important components of the model and presents highlights from our model evaluation process (full details are available in Zafarani (2013)). This project focused on two-dimensional networks in which the individual links (or bonds) in the network consisted of two-dimensional variable aperture fractures. This resulted in three-dimensional flow fields that were similar in structure to numerous prior studies in simple two-dimensional networks where the bonds were represented as one-dimensional connections (e.g., Park et al., 2001).

Though our approach is generalizable to more complex network topologies, in this study, we used 2D bond percolation networks (Broadbent and Hammersley, 1957) to define fracture network connectivity. We first defined a regular lattice of nodes and then connect each pair of neighboring nodes with probability Pn. Thus, for $Pn = 1$ this results in a uniform fully connected lattice. The percolation threshold occurs at $Pn \sim 0.5$, which means that for $Pn \lesssim 0.5$ it is unlikely that a connected path through the network will exist. Figure 1 shows two samples of percolation network maps randomly generated by the model.

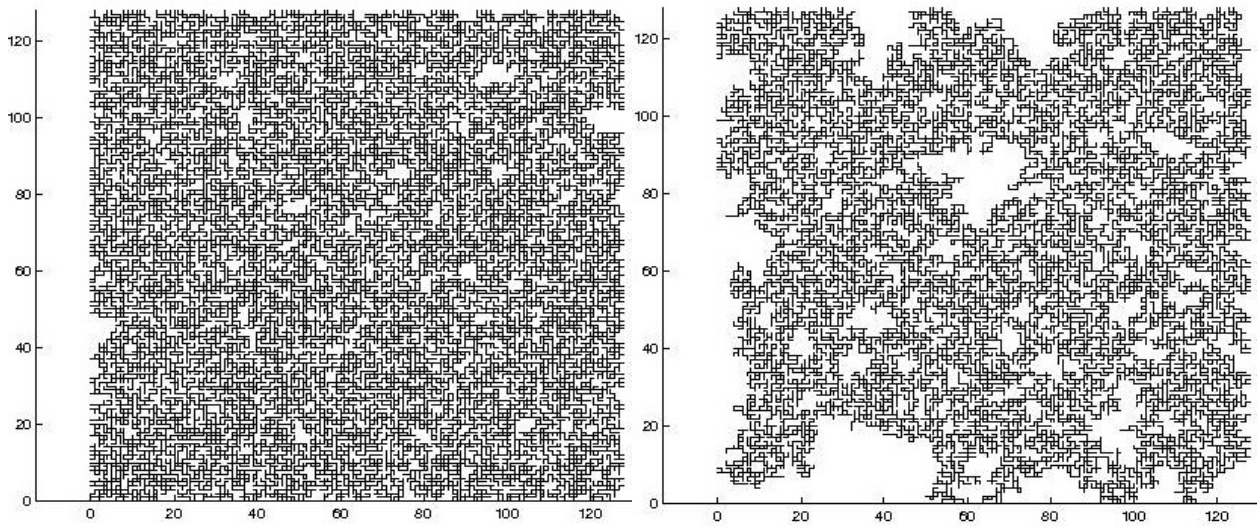

Figure 1: Samples of bond percolation networks. The size of network is 128×128 and Pn=0.52 (right) and Pn=0.6 (left) resulting in a maximum of 32768 fractures when $Pn = 1$.

We then extended the two-dimensional bond percolation networks to three dimensions by extruding each bond in the z-direction to create two-dimensional fractures. Each fracture includes small-scale aperture variability that represents observations of fracture apertures in natural fractures (Brown et al., 1995). Figure 2 shows an example of a variable-aperture discrete-fracture network, where the colors represent mean fracture aperture in the network-scale image and local aperture variability in the expanded image of two intersecting fractures.

Each fracture in the network consists of a synthetic correlated random aperture field generated using an approach proposed by Brown (1995). The power spectrum of aperture field is defined as:

$$\xi(\mathbf{k}) \;\propto\; \left(1 + \lambda^2 \left|\mathbf{k}\right|^2\right)^{-\left(\frac{1}{2}+H\right)} \tag{1}$$

where $\mathbf{k}$ is the wave number vector, H is the Hurst exponent, which is typically in the range $0.5 < H < 1$, and λ is a cutoff length scale. This functional form of $\xi(\mathbf{k})$ yields a smooth transition from the power law behavior ($|\mathbf{k}| > 1//lambda$) to the cutoff value ($|\mathbf{k}| < 1/\lambda$), which results in elimination of oscillations that occur with a abrupt cutoff. This characteristic of random field is referred to as well behaved semivariograms, with the cutoff value reflecting the length scale above which the two fracture surfaces are well matched.

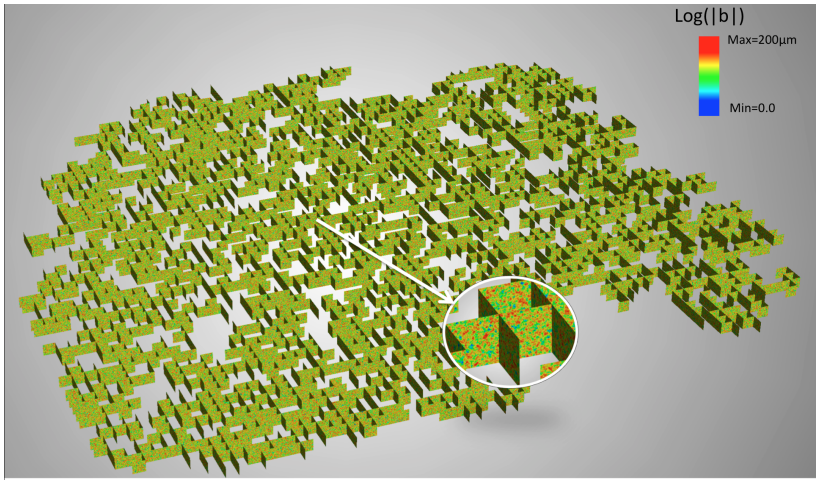

Figure 2: Example of a variable aperture discrete fracture network. Each fracture includes aperture variability as depicted in blown up segment of the network.

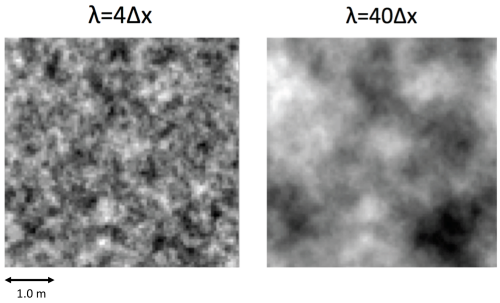

Figure 3: Sample of variable-aperture fractures generated for λ=4 and 40, where λ is the cutoff length scale associated with Eq. 1.

2.1 Flow model

Our computational model explicitly represents preferential flow within each fracture induced by aperture variability. Thus, the basic building block for the model is a single variable-aperture fracture. These single fractures are then connected at fracture intersections such that mass and momentum are conserved throughout the fracture network. Here we first present the single fracture model and then discuss how these single fractures are linked within the discrete fracture network.

Flow through the three-dimensional void space between rough fracture surfaces is governed by the Navier-Stokes equations:

$$\rho \left(\frac{\partial \mathbf{u}}{\partial t} + \mathbf{u} \cdot \nabla \mathbf{u} \right) = \mathbf{F} - \nabla p + \mu \nabla^2 \mathbf{u} \tag{2}$$

where ρ is the fluid density, $\mathbf{F}$ is the body force vector (per unit mass), p is pressure, μ is the fluid viscosity, and $\mathbf{u}$ is the velocity vector. The left-hand-side quantifies the acceleration of a fluid parcel along its trajectory and the terms on the right-hand side represent the sum of applied body forces, applied pressure gradient, and viscous forces. For

an incompressible fluid, mass conservation also dictates that:

$$\nabla \cdot \mathbf{u} = 0 \tag{3}$$

In subsurface flows, gravity is the acting body force, so $\mathbf{F} = g$, which can be combined with p by defining $P = p + \rho g z$. Furthermore, for low-Reynolds-number flows, typical in the subsurface, the acceleration (or inertial) terms can be neglected and the resulting steady-state flow equation reduces to the Stokes equation:

$$\nabla P = \mu \nabla^2 \mathbf{u} \tag{4}$$

For the case of a parallel-plate fracture, pressure gradients across the fracture aperture (z-direction) reduce to zero and this equation simplifies to the Reynolds equation or local cubic law :

$$\mathbf{q} = \frac{-b^3 g}{12\nu} \nabla h \tag{5}$$

where $\mathbf{q}$ is the flow rate per unit width through a segment of fracture with aperture b and $h = P/\rho g$ is the hydraulic head. We apply the local cubic law to calculate flow within variable-aperture fractures by assuming that (5) holds locally despite variations in b. Finally, mass conservation requires that:

$$\nabla \cdot \mathbf{q} = 0 \tag{6}$$

Numerous studies over the past two decades have explored the appropriateness of (5) for representing flows through variable-aperture fractures (e.g., Zimmerman and Bodvarsson, 1996; Nicholl et al., 1999; Yeo and Ge, 2005; Brush and Thomson, 2003). Though aperture variability induces pressure gradients in the z-direction, Brush and Thomson (2003) demonstrated through detailed comparisons with Navier-Stokes based simulations and local-cubic-law simulations that (5) captures preferential flow patterns and bulk flow rates reasonably well if $Re < 1$, $Re\langle b \rangle / \lambda_b < 1$, and $Re\sigma_b / \langle b \rangle < 1$, where $Re = \rho \mathbf{q}/\mu$, $\langle b \rangle$ is the mean fracture aperture, λ_b and σ_b are the correlation length and standard deviation of aperture variability.

We discretize fractures within a fracture network into square grid blocks with uniform b. Applying (5) and (6) to variable aperture fractures requires an approximation for the effective aperture between adjacent grid blocks with different aperture. We use the harmonic average:

$$b^3_{i+1/2} = \frac{2 b_i^3 b_{i+1}^3}{b_i^3 + b_{i+1}} \tag{7}$$

Nicholl et al. (1999) compared simulations using a range of different approximations for $b^3_{i+1/2}$ and found this scheme resulted in the best agreement between simulations and experimental observations.

Within individual fractures, boundary conditions can be applied around the edges of the fracture. These are typically no-flow (i.e., $\nabla h \cdot \mathbf{n} = 0$, where $\mathbf{n}$ is a unit vector normal to the boundary) or constant head boundaries. However, within a fracture network, many fractures may not intersect a boundary, but will intersect other fractures within the network. To represent fracture intersections, we define a connected line of grid blocks within one of the intersecting fractures as intersection grid blocks. These grid blocks are then connected to the neighboring grid block within each of the intersecting fractures and continuity is enforced by specifying that $\sum_{i=1}^{n} \mathbf{q_i} = 0$ where n is the number of fractures connected to the intersection grid block (Figure 4). This approach to discretizing the

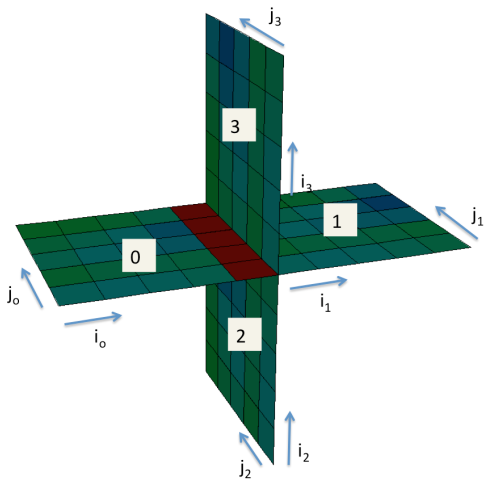

Figure 4: Simple 4-fracture network with 4-way fracture intersection. In this case the intersection node belongs to Fracture 0 (F0) and links are established between each of the neighboring fractures. Intersection nodes (red) are connected to the corresponding grid block in each fracture (F0, F1, F2, and F4).

fracture network allows us to define a local coordinate system within each fracture with communication between connected fractures only occurring at intersection nodes. Thus, this approach is readily parallelized by assigning individual fractures to individual computational processes and establishing communication between processes only at intersection grid blocks. Using Message Passing Interface (MIP), we parallelized this algorithm following an approach originally proposed by (Detwiler et al., 2006). At the fracture-network scale, we impose either constant h or no-flow boundaries and develop a system of equations that we solve implicitly for h throughout the entire fracture network. We then use (5) with the calculated values of h to calculate $\mathbf{q}$ throughout the fracture network, which is then used as input to large-scale solute transport simulations.

2.2 Solute Transport Model

Transport within fractured rock mass is governed by the three-dimensional advection-diffusion equation:

$$\frac{\partial c}{\partial t} + \mathbf{u} \cdot \nabla c = D_m \nabla^2 c \tag{8}$$

where c is the solute concentration and D_m is the molecular diffusion coefficient. We simplify this problem by neglecting advective transport in the rock matrix such that advection occurs only through the variable-aperture fractures. Though we do not explicitly solve for the three-dimensional velocity field within each fracture, $\mathbf{u}$, a reasonable approximation is to assume a parabolic velocity profile between the fracture surfaces, with the local average velocity defined as $\bar{\mathbf{u}} = \mathbf{q}/b$. This assumption is consistent with the assumption of negligible z-direction pressure gradients used to develop the flow model and is, thus, likely subject to similar constraints. The resulting quasi-three-dimensional velocity field is then:

$$\mathbf{u} = \frac{3}{2}(1 - 4z^2)\bar{\mathbf{u}} \tag{9}$$

where $-b/2 < z < b/2$.

Rather than develop an Eulerian discretization of (8), we use a Lagrangian approach that tracks particles subjected to advective and diffusive displacements within each time step as they travel through the interconnected fractures. When a particle enters the rock matrix by diffusion, the residence time in the rock matrix is described by an appropriate probability density function (described below). The particle-tracking approach has two primary advantages: 1) it does not introduce numerical diffusion, which is a persistent challenge with Eulerian solutions to advective processes and 2) it is able to quantify the impact of low-velocity, low-probability pathways through the fracture network on solute breakthrough curves.

Each three-dimensional particle displacement step is calculated as:

$$\Delta\mathbf{x} = \mathbf{u}\Delta t + \mathbf{w}\sqrt{2D_m\Delta t} \tag{10}$$

where $\mathbf{w}$ is a three-dimensional vector of random numbers drawn from a Gaussian probability density function with zero mean and unit variance. We use bilinear interpolation to estimate local velocities between grid-block faces.

2.2.1 Transport within fractures

Adaptive time stepping ensures that particles do not experience large velocity gradients during any single displacement. Velocity gradients occur in the fracture plane due to aperture variability and across the fracture aperture due to the imposed parabolic velocity profile. Thus, two criteria are needed to determine each time step, one that limits the displacement across the fracture aperture to a small fraction of the fracture aperture and one that limits displacements in the x-y plane to a fraction of a grid block.

Reimus and James (2002) noted that by defining a constraint on diffusive time steps, many diffusive displacements may be arbitrarily small. They thus developed a time-domain approach that rather specifies a fixed displacement and then selects the corresponding time step from a probability density function (pdf) of travel times. They simplified the resulting series solution by developing an empirical relationship for the resulting pdf. We apply this

approach by defining a maximum z-displacement of $0.05b$, which results in a diffusive time step of:

$$\Delta t_d = 0.376 \frac{(0.05b)^2}{D_m} \exp[0.787 \cdot \mathbf{w}] \tag{11}$$

where $\mathbf{w}$ is a zero-mean, unit-variance, normally-distributed random number.

We then select a maximum displacement in the $x-y$ plane of $0.5\Delta x$, where Δx is the grid spacing, which results in an advective time step of:

$$\Delta t_a = \frac{|\mathbf{u}|}{0.5\Delta x} \tag{12}$$

The time step for each displacement is then selected as $\min(\Delta t_a, \Delta t_d)$.

The transport model outlined to this point provides a means for tracking particles through individual rough-walled fractures and has been demonstrated to capture fracture-scale transport processes reasonably well (e.g., Detwiler et al., 2000). However, simulating transport through a fracture network requires an approach for routing particles through fracture intersections. Previous efforts to simulate transport through fracture intersections have assumed either complete mixing within the fracture intersection (Smith and Schwartz, 1984) or stream tube routing (Endo et al., 1984; Hull et al., 1987). In the case of complete mixing, the intersection acts as a mixer such that all fluid leaving the intersection has the same solute concentration, whereas stream tube routing assumes zero mixing within the intersection and assigns mass fluxes leaving the intersection as corresponding weighted averages of the incoming fluxes. High-resolution simulations using direct solutions to the Stokes equations through idealized fracture intersections (Mourzenko et al., 2002) show that the mixing that occurs within the fracture intersections is dependent upon the Peclet number ($Pe = \mathbf{q}/D_m$). The amount of mixing ranges from complete mixing in the diffusive limit ($Pe \to 0$) to streamtube routing ($Pe \to \infty$).

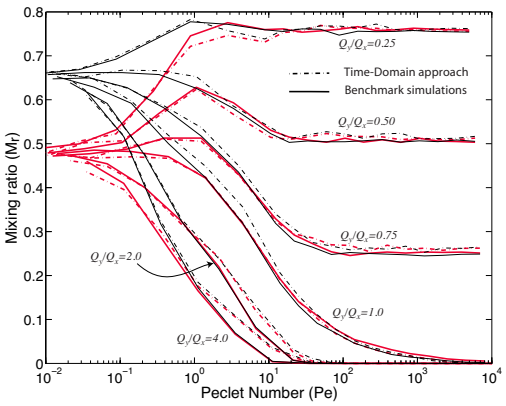

Figure 5: Mixing ratio at fracture intersections for Pe ranging from the diffusive limit (left side) to the advective limit (right side). Our newly proposed time-domain random walk approach accurately represents the Pe-dependent behavior observed in our high-resolution, Navier-Stokes-based benchmark simulations.

In order to represent the range of intersection mixing observed in these studies in our network-scale solute transport model, we developed an efficient approach for routing

particles through each intersection that does not require explicit calculation of the velocity field within the fracture intersection (Zafarani and Detwiler, 2013). The model uses a time-domain random walk approach and idealized representations of the velocity field within the fracture intersection to determine the path of particles through a fracture intersection in a single step. We evaluated the intersection mixing model by comparing simulation results to high-resolution mechanistic simulations in which we solved the Stokes equations for different intersection geometries and transported particles through the intersection. Calculated mixing ratios, $M_r =$ for $10^{-2} < Pe < 10^4$ exhibit excellent agreement over the entire range indicating the robustness of our new intersection transport model (Figure 5).

2.2.2 Transport within the rock matrix

Diffusive particle displacements perpendicular to the fracture plane occasionally result in particles intersecting the fracture surface. At each of these events, the probability that the particle enters the fracture matrix is given by:

$$P_{matrix} = \frac{\phi\sqrt{D_{me}}}{\sqrt{D_m} + \phi\sqrt{D_{me}}} \tag{13}$$

where D_{me} is the effective diffusion coefficient in the rock matrix and ϕ is the rock porosity. Once a particle enters the matrix, it is necessary to calculate both the time spent in the matrix before reentering the fracture and the displacement, $\mathbf{\Delta x}$ of the particle in the x-y plane of the fracture. To calculate the residence time within the rock matrix we approximate the fracture surface as a plane and select the first arrival time at the plane from the probability density function:

$$\Delta t_{matrix} = \frac{\Delta z_o^2}{2D_{me}\mathbf{w}^2} \tag{14}$$

where Δz_o is the distance into the matrix from the fracture surface, or the endpoint of the previous displacement of magnitude Δz, which is given by:

$$\Delta z_o = \sqrt{\frac{D_{me}(\Delta t - \Delta t_{fracture})}{D_m \Delta t}} \tag{15}$$

where $\Delta t_{fracture}$ is the portion of the previous time step spent in the fracture. The location at which the particle reenters the fracture can then be drawn from a probability density function representing the two-dimensional diffusion equation:

$$\mathbf{\Delta x} = \mathbf{w}\sqrt{2D_{me}\Delta t_{matrix}} \tag{16}$$

where $\mathbf{w}$ is a vector of zero-mean, unit-variance random numbers.

3 Summary of major results

We carried out parametric studies in large-scale fracture networks to explore the influence on network-scale transport behavior of: i) aperture variability within individual fractures; ii) configuration of solute injection; and iii) measurement scale. Following is a summary of key findings from these studies.

We selected network properties to reflect the field-scale tracer tests reported by (e.g., Zhou et al., 2007) and used small-scale aperture variability consistent with measurements of Brown (1995). We used values of percolation number, Pn, ranging from the percolation threshold to a uniform lattice. We generated correlated random aperture fields with $H = 0.8$, $\overline{b} = 3 \times 10^{-4}$ (m), cutoff lengths of $\lambda = 4\Delta x$ and 40Δ and standard deviation of $\sigma = 6.0 \times 10^{-5}$ (m). In each case we also considered the case of uniform fractures ($\sigma = 0$) to directly assess the effect of small-scale aperture variability on network-scale transport processes. Simulations proceeded for a total time of 50 years.

In addition, we tested two source configurations: (1) point source injection and (2) uniform concentration in the inflow boundary fractures. These conditions represent idealizations of a localized tracer test in which solute is introduced into a single fracture and release of a contaminant over a larger area, which is an idealization of a typical contaminant source zone. For the point source injection we initialized particles in a single fracture and flux weighted their locations across the width of the fracture to represent a uniform concentration. We chose the fracture for injection to coincide with flux-weighted middle of the inlet boundary of the fracture network, so that injected particles are hydraulically equidistant from the two no flow boundaries located on top and bottom of the network (Figure 6).

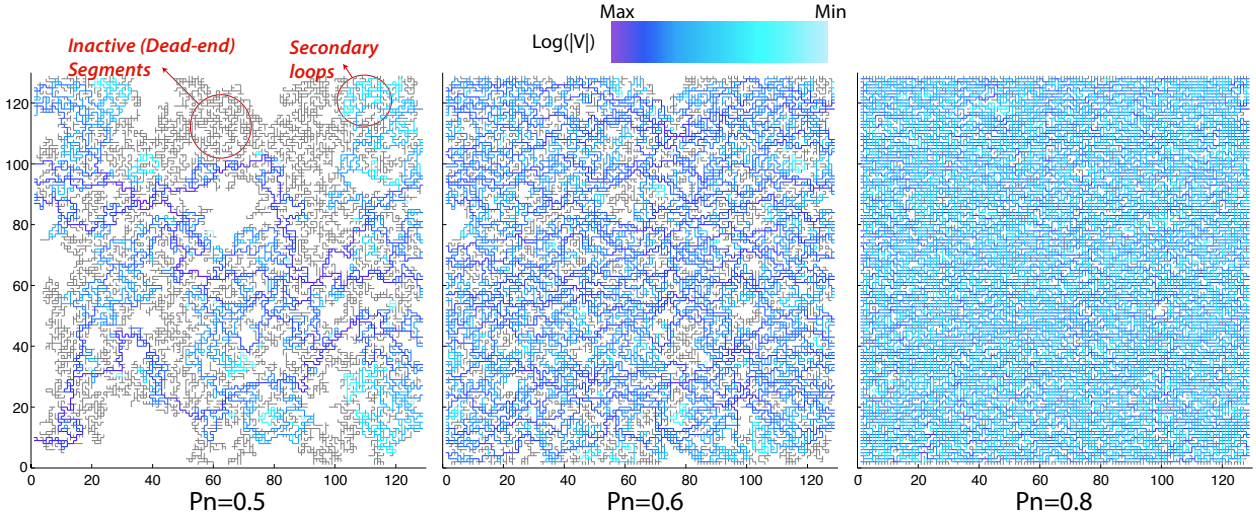

Figure 6: Cross-sections of fracture networks at different values of Pn. The color scale represents the mean flow velocity through each fracture on a logarithmic scale. Gray regions indicate fractures that are hydraulically connected to the boundaries but have a mean velocity of zero.

The distribution of flow rates exhibited a strong dependence on the connectivity of the

network (Figure 6). Purple regions indicate preferential pathways through the network where mean velocities are significantly larger than in the remainder of the fractures in the network. These fractures lie on pathways that are hydraulically well connected to the constant-head boundaries on the left and right of each network. For $Pn = 0.8$ the purple fractures are largely aligned with the mean flow direction (left to right), but as Pn decreases, the preferential pathways become more tortuous. In addition, the secondary flow loops (light blue regions) become longer an more circuitous; at large Pn the secondary loops largely connect adjacent fractures where there is a small local gradient perpendicular to the regional gradient. When Pn decreases, the secondary loops largely connect to two different locations along one preferential pathway, where flow is driven through the secondary pathway (which is much longer than the preferential pathway) by the same local gradient. The gray regions indicate fractures that are hydraulically connected to the boundaries, but have a net flow of zero. In many studies of transport through fracture networks, such connected but inactive fractures are removed from the network to improve computational efficiency. Indeed in a two-dimensional fracture network this is reasonable because there is no driving force for flow through these dead-end fractures.

In three-dimensional fracture networks, aperture variability within individual fractures leads to local pressure gradients along fracture intersections. The result is that, even though the net flow through the fracture may be zero, the possibility for advection in and out of these no-flow regions exists. Figure 7 demonstrates this through an enlargement of the intersection of two fractures on the preferential flow path [1], a secondary fracture [2], and a dead-end fracture [3].

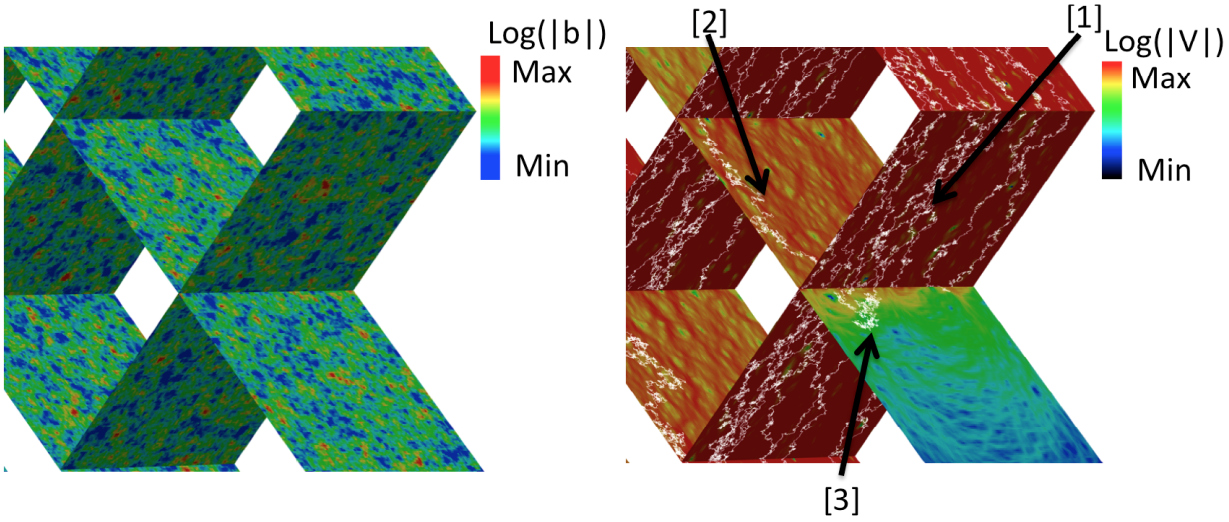

Figure 7: An example simulation highlighting key transport mechanisms in a variable-aperture fracture network. The figure shows fracture aperture (left) and flux with particle trajectories (right) and highlights three distinct transport regimes in the network: (1) Network-scale preferential flow paths; (2) Secondary loops that consist of connected fractures with non-zero flow; and (3) Dead-end fractures that are hydraulically connected to the boundaries on one end and thus have zero net flow. Advective loops in the are disconnected fracture caused by pressure gradients along the fracture intersection entrain particles into these dead-end fractures.

In the dead-end fracture [3], there is a sequence of advective loops that decrease in magnitude as the source and sink of the respective loops become further apart. Thus, these loops provide a localized scale-dependent mechanism for causing solute to enter and 'no-flow' fractures as can be seen by the white lines highlighting particle trajectories. Furthermore, because the velocities in these dead-end fractures are typically orders of magnitude less than those in the preferential and secondary fractures, diffusion contributes more significantly to transport than it does in the higher velocity flow paths.

Transport of particles into dead-end fractures leads to a significant increase in residence time for a fraction of the particles. Figure 8 shows breakthrough curves measured at the right-side boundary for particles released as a point source on the left-side boundary for networks consisting of fractures with different amounts of aperture variability. For

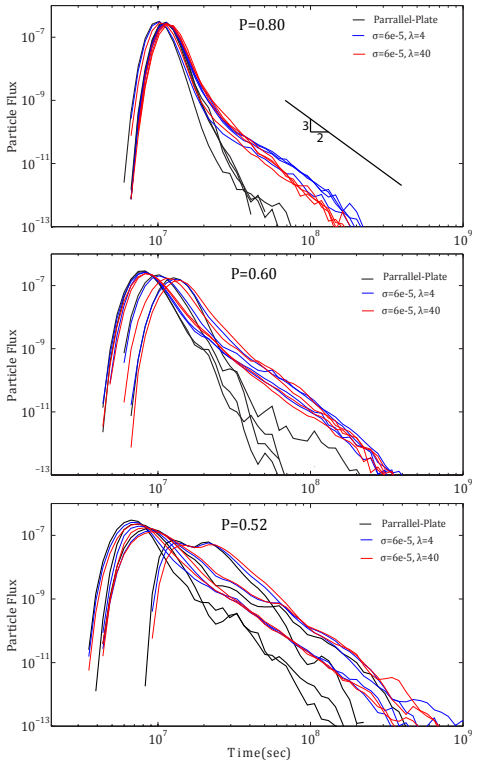

Figure 8: Breakthrough curves for four different network realizations. For each network realization, the network was populated with three different types of fractures: i) parallel-plate; ii) variable aperture with $\lambda = 4\Delta x$; and iii) variable aperture with $\lambda = 40\Delta x$.

networks consisting of parallel-plate fractures, pressure gradients along fracture intersections are nonexistent such that the results are identical to what would be predicted for a two-dimensional network. For the network with $Pn = 0.8$, the parallel-plate network results in near-Fickian behavior, while increasing aperture variability for the same network geometries leads to a significant increase in tailing. The breakthrough-curve tails exhibit slopes of about -3/2 as expected for the case of transport through fractures with matrix diffusion, but for these simulations $D_{me} = 0$ and $\phi = 0$ so there is no interaction with the

rock matrix. Thus, these results show that simply adding local aperture variability causes the transition away from a Fickian dispersion process. As the fracture networks become more sparse, the influence of aperture variability on the breakthrough curves becomes less significant and inter-realization variability increases, but the long-time behavior is consistent, in that the breakthrough-curve tails have a similar slope to that observed for the variable-aperture $Pn = 0.8$ networks.

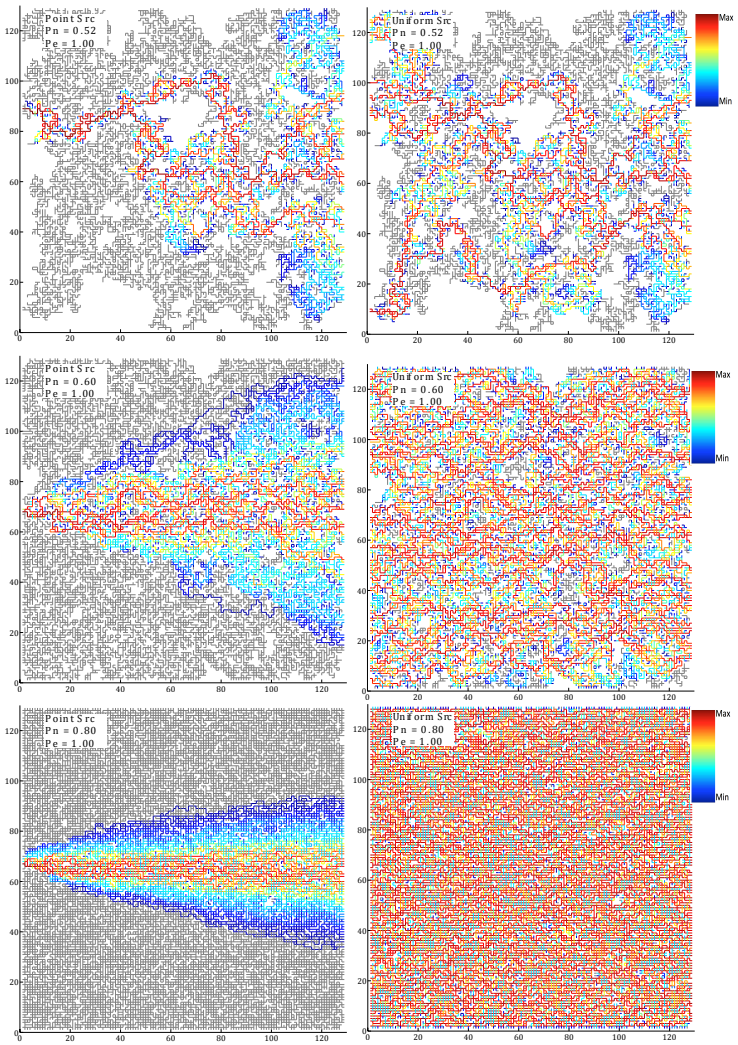

Figure 9: Trajectory of particles through networks with different values of Pn. The color scale reflects the relative number of particles that passed through each fracture in the network. The left-hand column used a point source injection of the particles and the right-hand column used a uniform flux-weighted source along the left-hand boundary through the same network. During these simulations, breakthrough curves were recorded at multiple distances from the source (Figure 10).

The length scale at which travel times are recorded and the type of source both influence interpretation of measured breakthrough curves. Figure 9 shows particle trajectories through a set of fracture networks with different values of Pn. For the case of $Pn = 0.8$ the tracer plume appears fairly uniform as one might expect from a Fickian dispersion process. However, as noted above, due to local aperture variability, the resulting

breakthrough curves are non-Fickian. As Pn and the connectivity of the network decreases, the tracer plume becomes more irregular and focused through a smaller number of preferential flow paths. In addition, particles are increasingly exposed to regions identified as secondary loops and dead-end fractures (Figure 6). The resulting breakthrough curves exhibit scale dependence and, to a lesser extent, a dependence upon the type of boundary condition (Figure 10). At short length scales, the breakthrough curves exhibit multiple peaks at early time and a -3/2 slope characteristic of matrix diffusion. However, as the distance from the source plane increases, the initial peaks in the breakthrough curves become smoother because particles have the opportunity to sample more fractures with a broader range of mean velocities. In addition, in all cases, at larger scales, the power-law slope of the breakthrough-curve tails increases. This effect is more pronounced for the point source simulations.

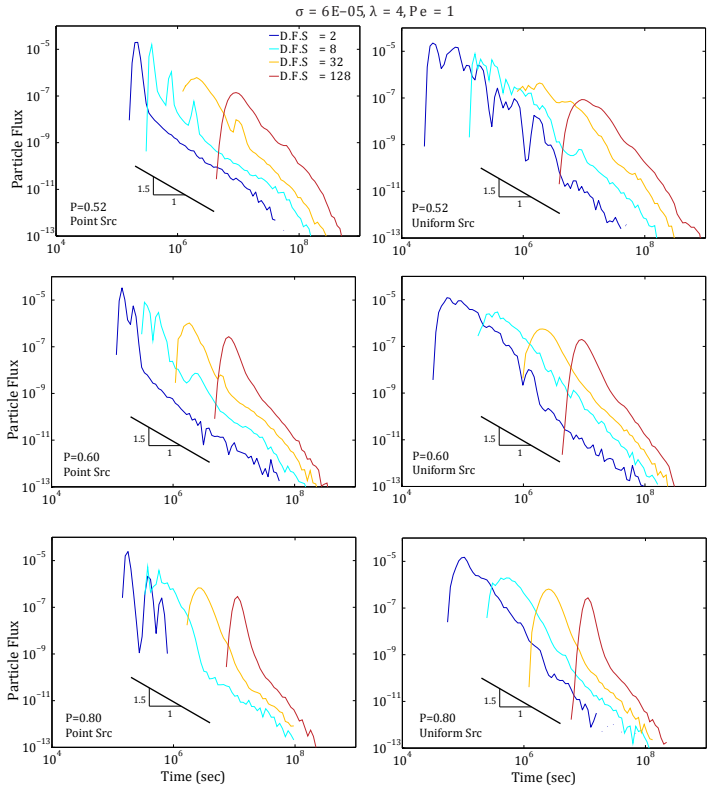

Figure 10: Breakthrough curve results for a network with P=0.52 are shown for distances from source (D.F.S) ranging from 2 to 128 meters. Solid line indicates slope 3/2 (log-log scale), which is suggested as indicator of matrix diffusion in fracture networks. Point source injection results in closer distances from source shows slopes close to $-3/2$. Results of uniform injection (left) and point source injection (right) show key differences in slope in small scale, while In larger scales their slope converges to the same value.

4 Conclusions

During this project, we developed and tested a model of variable-aperture solute transport in discrete fracture networks (VAST-DFN). The model is parallelized to allow direct simulation of small-scale transport processes in fracture networks consisting of $O(10^5)$ fractures spanning 100s of meters. The model includes diffusion into the rock matrix, but our results to date have focused on the transport processes occurring within the fractures. In addition, we developed a new particle-tracking-based approach for simulating solute transport through fracture intersections. The model predicts the Pe-dependent nature of transport through intersections without the need for high-resolution calculation of the velocity field within the fracture intersections. This allows a rigorous representation of fracture intersections in large-scale fracture networks where high-resolution calculation of the velocity fields within each intersection is not computationally feasible.

We used simulations in a series of large-scale fracture networks with characteristics (length scale, fracture connectivity, aperture variability) representative of previously reported field-scale tracer tests (Zhou et al., 2007) to explore the mechanisms responsible for observations of scale dependence of parameters fitted during tracer tests. Our results show that small-scale aperture variability can lead to enhanced tailing of breakthrough curves even in the absence of matrix diffusion. These results provide a mechanistic explanation for the observed scale dependence of fitted effective matrix diffusion coefficient and highlight the importance of developing upscaled models that effectively represent the mechanisms that lead to long-tailed breakthrough curves: (i) diffusion in and out of the rock matrix; (ii) advection-driven transport in and out of dead-end fractures; and (iii) advective transport within secondary flow channels.

Though the simulations carried out during this project involved somewhat idealized fracture networks, we still observed the scale-dependent, non-Fickian dispersion commonly observed in field-scale data. Thus, these simulations present an important step towards developing a mechanistic basis for upscaled models of solute transport in large-scale fracture networks. However, the ability to represent a broad range of network topologies is clearly necessary to fully realize the connection between the mechanisms controlling transport through fracture networks and field-scale observations. An outstanding question is the role of fracture intersections in transport processes. Our three-dimensional networks, generated by extruding a two-dimensional network in the third dimension, result in regional pressure gradients that are always perpendicular to the fracture intersections. In the other limit, in which pressure gradients are parallel to fracture intersections, the influence of fracture intersections will be quite different as the intersections will become localized preferential flow paths. Our modeling approach provides a mechanistic approach to explore the influence of this transition in more complex network geometries.

This project was part of a collaboration with the University of Colorado, Boulder where they developed robust upscaled models of solute transport through single fractures. During this project, we began integrating their upscaled model into our discrete fracture network model. Using the upscaled approach, it is unnecessary to explicitly represent three-dimensional transport within each fracture, which greatly enhances the

computational efficiency of the model with no measurable degradation in the accuracy of the simulation results. As a result, this upscaled approach promises to allow field-scale simulations in discrete fracture networks at a fraction of the computational run times required for our high-resolution model.

5 Publications and presentations citing support from this project

5.1 Publications

Zafarani, A. and Detwiler, R. L. (2013). An efficient time-domain approach for simulating pe-dependent transport through fracture intersections, *Advances in Water Resources*, 53:198-207.

Zafarani, A. and Detwiler, R. L. (to be submitted). Solute transport in discrete fracture networks: The role of small-scale aperture variability on network-scale transport processes, *Water Resources Research*.

Zafarani, A. (2013). High-Resolution Analyses Of Anomalous Transport In Large-Scale Variable-Aperture Discrete Fracture Networks. PhD thesis, University of California, Irvine.

5.2 Presentations

Zafarani, A. and Detwiler, R. L., American Geophysical Union Fall Meeting, "Solute transport in three-dimensional variable-aperture discrete fracture networks," San Francisco, California. (December 3, 2012 - December 7, 2012).

Zafarani, A. and Detwiler, R. L., American Geophysical Union Fall Meeting, "Solute transport through fracture intersections: An efficient time-domain random-walk algorithm," San Francisco, California. (December 5, 2011 - December 9, 2011).

Detwiler, R. L. and Zafarani, A., Engineering Mechanics Institute 2010, "Numerical modeling of solute transport at fracture intersections," University of Southern California, Los Angeles, California. (August 8, 2010 - August 11, 2010).

References

Becker, M. W. and Shapiro, A. M. (2000). Tracer transport in fractured crystalline rock: Evidence of nondiffusive breakthrough tailing. *Water Resour. Res.*, 36(7):1677–1686.

Broadbent, S. R. and Hammersley, J. M. (1957). Percolation processes. *Math. Proc. Cambridge Philos. Soc.*, 53(03):629–641.

Brown, S. R. (1995). Simple mathematical model of a rough fracture. *J. Geophys. Res.-Sol. Ea.*, 100(B4):5941–5952.

Brown, S. R., Stockman, H. W., and Reeves, S. J. (1995). Applicability of the reynolds equation for modeling fluid flow between rough surfaces. *Geophys. Res. Lett.*, 22(18):2537–2540.

Brush, D. J. and Thomson, N. R. (2003). Fluid flow in synthetic rough-walled fractures: Navier-stokes, stokes, and local cubic law simulations. *Water Resour. Res.*, 39(4):n/a–n/a.

Callahan, T. J., Reimus, P. W., Bowman, R. S., and Haga, M. J. (2000). Using multiple experimental methods to determine fracture/matrix interactions and dispersion of nonreactive solutes in saturated volcanic tuff. *Water Resour. Res.*, 36(12):3547–3558.

Dai, Z. X., Wolfsberg, A., Reimus, P., Deng, H. L., Kwicklis, E., Ding, M., Ware, D., and Ye, M. (2012). Identification of sorption processes and parameters for radionuclide transport in fractured rock. *J. Hydrol.*, 414:220–230.

Dearden, R., Noy, D., Lelliott, M., Wilson, R., and Wealthall, G. (2013). Release of contaminants from a heterogeneously fractured low permeability unit underlying a {DNAPL} source zone. *Journal of Contaminant Hydrology*, 153(0):141 – 155.

Detwiler, R., Rajaram, H., and Glass, R. (2000). Solute transport in variable-aperture fractures: An investigation of the relative importance of taylor dispersion and macrodispersion. *Water Resour. Res.*, 36(7):1611–1625.

Detwiler, R. L., Morris, J. P., and Ezzedine, S. M. (2006). Coupling micromechanics and fluid flow through discrete fracture networks: Quantifying effective permeability under variable stress conditions. In *Eos Trans. AGU, 87(52)*, Fall Meet. Suppl., Abstract H13D-1433.

Endo, H., Long, J., Wilson, C., and Witherspoon, P. (1984). A model for investigating mechanical transport in fracture networks. *Water Resour. Res.*, 20(10):1390–1400.

Grisak, G. E. and Pickens, J. F. (1981). An analytical solution for solute transport through fractured media with matrix diffusion. *J. Hydrol.*, 52(1-2):47–57.

Hodgkinson, D., Benabderrahmane, H., Elert, M., Hautojarvi, A., Selroos, J.-O., Tanaka, Y., and Uchida, M. (2009). An overview of task 6 of the aspo task force: modelling groundwater and solute transport: improved understanding of radionuclide transport in fractured rock. *Hydrogeol. J.*, 17(5):1035–1049.

Hoehn, E., Eikenberg, J., Fierz, T., Drost, W., and Reichlmayr, E. (1998). The grimsel migration experiment: field injection–withdrawal experiments in fractured rock with sorbing tracers. *J. Contam. Hydrol.*, 34(1–2):85–106.

Hull, L., Miller, J., and Clemo, T. (1987). Laboratory and simulation studies of solute transport in fracture networks. *Water Resour. Res.*, 23(8):1505–1513.

Jardine, P. M., Sanford, W. E., Gwo, J. P., Reedy, O. C., Hicks, D. S., Riggs, J. S., and Bailey, W. B. (1999). Quantifying diffusive mass transfer in fractured shale bedrock. *Water Resour. Res.*, 35(7):2015–2030.

Kurtzman, D., Nativ, R., and Adar, E. M. (2007). Flow and transport predictions during multi-borehole tests in fractured chalk using discrete fracture network models. *Hydrogeol. J.*, 15(8):1629–1642.

Maloszewski, P. and Zuber, A. (1985). On the theory of tracer experiments in fissured rocks with a porous matrix. *J. Hydrol.*, 79(3-4):333–358.

Maloszewski, P. and Zuber, A. (1990). Mathematical modeling of tracer behavior in short-term experiments in fissured rocks. *Water Resour. Res.*, 26(7):1517–1528.

Maloszewski, P., Zuber, A., Bedbur, E., and Matthess, G. (2003). Transport of three herbicides in ground water at twin lake test site, chalk river, ontario, canada. *Ground Water*, 41(3):376–386.

Mourzenko, V. V., Yousefian, F., Kolbah, B., Thovert, J. F., and Adler, P. M. (2002). Solute transport at fracture intersections. *Water Resour. Res.*, 38(1):1000.

Neretnieks, I. (1980). Diffusion in the rock matrix: An important factor in radionuclide retardation? *J. Geophys. Res.-Sol. Ea.*, 85(B8):4379–4397.

Nicholl, M. J., Rajaram, H., Glass, R. J., and Detwiler, R. (1999). Saturated flow in a single fracture: evaluation of the reynolds equation in measured aperture fields. *Water Resour. Res.*, 35(11):3361–3373.

Novakowski, K. S. and Lapcevic, P. A. (1994). Field measurement of radial solute transport in fractured rock. *Water Resour. Res.*, 30(1):37–44.

Park, Y., Lee, K., and Berkowitz, B. (2001). Effects of junction transfer characteristics on transport in fracture networks. *Water Resour. Res.*, 37(4):909–923.

Park, Y., Lee, K., Kosakowski, G., and Berkowitz, B. (2003). Transport behavior in three-dimensional fracture intersections. *Water Resour. Res.*, 39(8):1215.

Rasmuson, A. and Neretnieks, I. (1981). Migration of radionuclides in fissured rock: The influence of micropore diffusion and longitudinal dispersion. *J. Geophys. Res.-Sol. Ea.*, 86(B5):3749–3758.

Reimus, P. and James, S. (2002). Determining the random time step in a constant spatial step particle tracking algorithm. *Chem. Eng. Sci.*, 57(21):4429–4434.

Reimus, P., Pohll, G., Mihevc, T., Chapman, J., Haga, M., Lyles, B., Kosinski, S., Niswonger, R., and Sanders, P. (2003a). Testing and parameterizing a conceptual model for solute transport in a fractured granite using multiple tracers in a forcedgradient test. *Water Resour. Res.*, 39(12):1356.

Reimus, P. W., Duke, C. L., and Roback, R. C. (2011). Translation of field tracer-test results into bounding predictions of matrix diffusion in the shallow subsurface at idaho national laboratory, usa. *Hydrogeol. J.*, 19(5):1021–1037.

Reimus, P. W., Haga, M. J., Adams, A. I., Callahan, T. J., Turin, H. J., and Counce, D. A. (2003b). Testing and parameterizing a conceptual solute transport model in saturated fractured tuff using sorbing and nonsorbing tracers in cross-hole tracer tests. *J Contam Hydrol*, 62-63:613–36.

Smith, L. and Schwartz, F. W. (1984). An analysis of the influence of fracture geometry on mass transport in fractured media. *Water Resour. Res.*, 20(9):1241–1252.

Tang, D., Frind, E., and Sudicky, E. A. (1981). Contaminant transport in fractured porous media: Analytical solution for a single fracture. *Water Resour. Res.*, 17(3):555–564.

Wang, Z., Rutqvist, J., and Dai, Y. (2013). A Multi-continuum Method for Studying the Effect of Inactive Fractures on Solute Transport in 2-D Discrete Fracture Network. *CMES Comput Model Eng Sci.* , 92(6):539–556.

Yeo, I. and Ge, S. (2005). Applicable range of the reynolds equation for fluid flow in a rock fracture. *Geosci. J.*, 9(4):347–352.

Zafarani, A. (2013). *High-Resolution Analyses Of Anomalous Transport In Large-Scale Variable-Aperture Discrete Fracture Networks*. PhD thesis, University of California, Irvine.

Zafarani, A. and Detwiler, R. L. (2013). An efficient time-domain approach for simulating pe-dependent transport through fracture intersections. *Adv. Water Resour.*, 53:198–207.

Zhou, H. and Xie, H. (2003). Direct estimation of the fractal dimensions of a fracture surface of rock. *Surf. Rev. Lett.*, 10(5):751–762.

Zhou, Q., Liu, H.-H., Molz, F. J., Zhang, Y., and Bodvarsson, G. S. (2007). Field-scale effective matrix diffusion coefficient for fractured rock: Results from literature survey. *J. Contam. Hydrol.*, 93(1-4):161–187.

Zimmerman, R. W. and Bodvarsson, G. S. (1996). Hydraulic conductivity of rock fractures. *Transport Porous Med.*, 23(1):1–30.